Journal of Materials Chemistry A

ROYAL SOCIETY OF CHEMISTRY

PAPER

View Article Online
View Journal

Cite this: DOI: 10.1039/d6ta00849f

Enhanced activity and durability of Ir single-atom catalysts for the electrocatalytic oxygen evolution reactions through synergistic electronic coupling with Co_3O_4 matrix

Astha Gupta,[a] Swarup Ghosh,[b] Dinesh Bhalothia,*[c] Joydeep Chowdhury[d] and Surojit Pande*[a]

Single-atom catalysts (SACs), owing to their high activity, selectivity, and 100% atom economy, show great potential for heterogeneous catalysis. However, their synthesis is still a challenge because of their poor stability and low tendency to aggregate. In this regard, we propose an approach for synthesizing a stable Ir single-atom catalyst on a Co_3O_4 substrate using a hydrothermal technique followed by calcination. The XAS and XPS analyses revealed the strong electronic coupling between the Ir SAC and the support matrix, which stabilized the single atoms *via* the formation of Ir–O and Ir–Co bond pairs. The strong electronic interaction resulted in an enhanced density of unoccupied d-orbitals of Ir single atoms and a higher valence state of Co atoms, both of which synergistically improved the electrocatalytic activity. HAADF-STEM images confirmed the isolated homogeneous distribution of Ir single atoms on the Co_3O_4 matrix. The synthesized catalyst, Ir_{SAC}–Co_3O_4, showed improved activity for the electrocatalytic oxygen evolution reaction (OER) in 1 M KOH, with an overpotential of 270 mV and a Tafel slope value of 76 mV dec^{-1}. The Ir_{SAC}–Co_3O_4 catalyst exhibited a high electrocatalytic durability up to 96 hours at an elevated current density of 130 mA cm^{-2}, demonstrating the robust electronic interaction of single atoms with the support matrix, which prevented the aggregation of single atoms. Post-electrocatalytic XPS analysis revealed no substantial change in the valence state, which can be further accredited to the electronic coupling between the support and the single atom. DFT findings demonstrated that the presence of the Ir single atom promoted the OER kinetics by stabilizing the key reaction intermediates and lowering the overpotential of the rate-determining step.

Received 28th January 2026
Accepted 10th April 2026

DOI: 10.1039/d6ta00849f

rsc.li/materials-a

1. Introduction

In the current context, the most extensive energy conversion sources are fossil fuels. This excessive dependence not only causes their exhaustion but also raises environmental concerns. To solve this issue, it is necessary to search for cleaner, abundant and affordable energy sources as alternatives. In this context, one of the most renowned approaches for producing renewable and sustainable energy is electrocatalytic water splitting, which generates hydrogen and oxygen.[1,2] The OER process is a multi-step, four-electron exchange procedure with the underlying complex mechanism involving O–O coupling and O–H bond cleavage, which makes it sluggish in nature compared with the HER, involving a two-electron transfer procedure. Thus, the overall productivity of electrocatalytic water splitting suffers from the slow reaction kinetics of the anodic OER, leading to substantial energy loss, necessitating the design of an efficient OER electrocatalyst. Currently, IrO_2 and RuO_2 are the most extensively employed commercial electrocatalysts for the OER, but their scarcity and poor stability limit their widespread application.[3–5] Consequently, many efforts have been made to develop affordable alternative electrocatalysts, such as transition metal-based oxides[6,7] or hydroxides,[8,9] sulphides,[10,11] phosphides,[12,13] selenides,[14] and perovskite oxides,[15,16] for the OER. Nevertheless, their catalytic activity is inadequate and far less than the standard, requiring refinement to obtain substantial efficiency.

Single-atom catalysts (SACs) have garnered much consideration due to their electrocatalytic performance in heterogeneous catalysis, with many advantages such as enhanced homogeneity of active sites, improved activity, and maximum atom utilization.[17–21] Furthermore, the unsaturated

[a]Department of Chemistry, Birla Institute of Technology and Science, Pilani, Rajasthan-333031, India. E-mail: spande@pilani.bits-pilani.ac.in
[b]School of Computer Science and Artificial Intelligence, SR University, Warangal, Telangana 506371, India
[c]Department of Electronics and Communication Engineering, Manipal University Jaipur, Rajasthan 303007, India
[d]Department of Physics, Jadavpur University, 188, Raja S.C. Mallick Road, Kolkata, 700032, India

coordination states of isolated atoms maximize the metal atom utilization and lower the reaction energy barrier, thereby promoting efficient adsorption and activation of reactant molecules. However, the synthesis of SACs remains challenging due to their low metal loading and poor stability, leading to the aggregation of isolated atoms into either a nanoparticle or a cluster.[22,23] These isolated atoms can be mounted to a variety of supports, such as carbon-based materials,[24] metal phosphides,[25] layered double hydroxides[26] and metal oxides.[27]

Compared with the other types of support matrix, metal oxides have received extensive attention because of their distinctive properties such as their high stability, oxygen vacancies, and defect sites.[28,29] These sites work as anchored points for isolated atoms and provide strong metal–support interactions through the formation of M–M and M–O bonds between the isolated atoms and the metal oxide support matrix.[30,31] Moreover, under OER conditions, transition metal oxide supports can undergo dynamic surface reconstruction, leading to the formation of catalytically active (oxy)hydroxide layers. These reconstructed species are often considered the true active phase.[32,33] The presence of single atoms may facilitate this reconstruction process, which further contributes to the enhanced electrocatalytic activity.[34] In this regard, Kumar and co-workers[34] synthesized an Ir single atom on a NiO support, which exhibited a 256 mV overpotential value to generate a 10 mA cm^{-2} current density. The isolated Ir atoms are partly embedded on a NiO substrate *via* forming an Ir–O and Ir–Ni bond that provides the structural rigidity and prevents the aggregation of Ir single atoms. Moreover, under operating conditions, the active structure of the electrocatalyst was analyzed by *in situ* Raman spectroscopy, which reveals the formation of NiOOH for both NiO and Ir-decorated NiO. The formation of NiOOH occurs at a much lower potential for the Ir-decorated NiO in contrast to the pristine NiO, suggesting the metal-support interaction among the NiO support and isolated Ir atoms. Yang and co-workers[35] developed an Ir single-atom catalyst over an oxygen-vacant $CoNiO_2$ support as an effective electrocatalyst for the OER. The Ir single atoms show a higher valence state and form an Ir–O covalent bond, resulting in the substantial overlay of 5d and 2p bands of Ir and O, respectively, which boosts the O_2 evolution by accelerating the conversion from O–O to OO* by following the lattice oxygen mechanism pathway. Cai and co-workers[36] reported Ir single atoms supported on CoO_x nanosheets for the OER. The Ir atoms captured by surface-absorbed oxygen form an Ir–O–Co bond, stabilizing the isolated Ir atoms and promoting the electrocatalytic OER. Shan and co-workers[37] synthesized Ir single atoms that integrated into a Co_3O_4 spinel ($Ir_{0.06}Co_{2.94}O_4$) to provide an efficient electrocatalyst for the OER in 0.1 M $HClO_4$. Ir single atoms integrated into the Co_3O_4 *via* an ion exchange process followed by calcination using ZIF-67 as a source for Co_3O_4. The observed onset potential was 1.45 V *vs.* RHE, with high mass activity of 2511 A g^{-1}. The cooperative contribution of nanodomains, containing Ir in the octahedral sites enclosed within the Co sites, is attributed to the elevated activity. The incorporation and stabilization of a Ce single atom on a Co_3O_4 support *via* a Ce–O bond was reported by Zhao and co-workers[38] for the OER in acidic medium. The synthesized electrocatalyst exhibited an onset potential of 1.57 V *vs.* RHE at 10 mA cm^{-2} current density. The increased charge transportation and modified electronic environment post Ce single atom incorporation into Co_3O_4 were attributed to the enhanced activity. According to these observations reported in the literature, anchoring metal isolated atoms on a metal oxide support can effectively improve the electrocatalytic OER activity.

Inspired by the previous reports, we synthesized Ir single atoms supported on Co_3O_4 on carbon cloth (CC) *via* a hydrothermal process followed by pyrolysis. The synthesized catalyst demonstrated improved performance for the OER in 1.0 M KOH. Pristine Co_3O_4 and single-atom-decorated samples were intensively characterized using various techniques such as X-ray diffraction (XRD), high-angle annular dark field-scanning transmission electron microscopy (HAADF-STEM), X-ray absorption spectroscopy (XAS), and X-ray photoelectron spectroscopy (XPS). The optimized Ir SAC on Co_3O_4 showed superior electrocatalytic OER activity in an alkaline medium, achieving a current density of 10 mA cm^{-2} at an onset potential of 1.51 V *vs.* RHE, and a low Tafel slope value of 76 mV dec^{-1}. The following points briefly describe the positive outcome of this work: First, the formation method is simple and easy to comprehend, resulting in an Ir single atom loading of 3.02 wt% on a Co_3O_4 support. Second, the enhanced activity resulting from faster charge transfer can be attributed to the synergistic electronic coupling between the Ir single atoms and the Co_3O_4 substrate. Third, the as-synthesized Ir_{SAC}–Co_3O_4 shows remarkable stability in the OER. Fourth, the DFT results unveil the metallic character of Ir_{SAC}–Co_3O_4 with a zero band gap after the introduction of Ir, which facilitates the charge transfer and subsequently improves the electrocatalytic activity.

2. Experimental section

2.1. Synthesis of Co_3O_4

The synthesis of Co_3O_4 involved a hydrothermal method followed by calcination. First, $Co(NO_3)_2 \cdot 6H_2O$ (0.6 g) and NH_2-$CONH_2$ (0.6 g) were mixed in 30 mL of Milli-Q water. The entire solution was then transferred to an autoclave. The carbon cloth was cut into a suitable shape (4 × 3 cm) and placed in the autoclave to undergo an 8 hours hydrothermal reaction at 95 °C. In the first step, a metal-carbonate hydroxide precursor ($Co(CO_3)_x(OH)_y \cdot H_2O$) was developed over the CC surface. After washing with water and ethanol, the as-deposited CC was dried for 8 h at 50 °C. The resulting carbonate precursor grown on CC was calcined for 3 h at 350 °C in a muffle furnace to yield Co_3O_4 and used as a pristine sample.

2.2. Synthesis of Ir_{SAC}–Co_3O_4

The synthesis of single-atom Ir-doped Co_3O_4 was completed in two steps. The $Co(CO_3)_x(OH)_y \cdot H_2O$ precursor was initially synthesized over CC by following the hydrothermal method as discussed above. In the second step, the metal-carbonate hydroxide complex deposited over CC was impregnated into a solution of $IrCl_3$ xH_2O (3.15×10^{-2} M or 10 mg mL^{-1}) for 10

minutes, followed by drying and calcination at 350 °C for 3 h, to obtain Ir single-atom-doped Co_3O_4 (Ir_{SAC}–Co_3O_4). The amount of Ir precursor was optimized by varying the concentration of $IrCl_3$ xH_2O solution (5 mg mL^{-1}, 15 mg mL^{-1}, 20 mg mL^{-1} and 25 mg mL^{-1}), where the other reactant remained unchanged. The ICP analysis of all the samples obtained by varying the concentration of the Ir precursor solution is presented in Table S1 (SI). The data indicate that the Ir weight percentage on Co_3O_4 increases with the increasing concentration of $IrCl_3$ solution. The optimized sample exhibits an Ir content of 3.02 wt%.

2.3. Electrochemical measurements

The electrocatalytic activity of Ir_{SAC}–Co_3O_4 and Co_3O_4 was evaluated in 1 M KOH by a three-electrode system. The working electrode was prepared with the sample obtained (Co_3O_4 and Ir_{SAC}–Co_3O_4) on CC, while Ag/AgCl and a graphite rod were used as the reference and counter electrodes, respectively. The working electrode area (0.4 × 0.4 cm^2) was fixed by applying epoxy paste on the sample-deposited CC. The catalyst loading of Ir_{SAC}–Co_3O_4 and Co_3O_4 was 0.28 mg. All electrochemical investigations were performed using a CHI604E instrument. At a scan rate of 2.0 mV s^{-1}, a potential window of 0 to 0.8 V for the OER *vs.* Ag/AgCl was employed for the linear sweep voltammetry (LSV) analysis. The formula $E_{RHE} = E_{Ag/AgCl} + 0.0591 \times pH + E^0_{Ag/AgCl}$ was employed to convert the potential of the Ag/AgCl reference electrode to the RHE scale. In the electrochemical impedance spectroscopy (EIS) analysis of Ir_{SAC}–Co_3O_4 and pristine Co_3O_4, the onset potential was used as an operational bias for data recording.

3. Results and discussion

3.1. Mechanism of synthesis

The experimental section explained the complete synthesis of Ir single atoms anchored over Co_3O_4. In the first step, *i.e.*, hydrothermal process, the metal-carbonate hydroxide precursor ($Co(CO_3)_x(OH)_y \cdot H_2O$) was formed. First, the hydrolysis of urea released CO_3^{2-} and OH^-, which then reacted with Co^{2+} to form a metal-carbonate hydroxide precursor. In the second step, the metal-carbonate hydroxide precursor was converted into Co_3O_4 by calcination for 3 h at 350 °C. To synthesize Ir_{SAC}–Co_3O_4, the metal–carbonate–hydroxide complex was impregnated into the $IrCl_3$ xH_2O solution to enable the electrostatic adsorption of Ir-ions on the precursor surface, followed by drying and calcination for 3 h at 350 °C. The overall synthesis strategy for Ir_{SAC}–Co_3O_4 is given in Scheme 1. The plausible reaction mechanism involved in the formation of Co_3O_4 is as follows:

$$H_2NCONH_2 + H_2O \rightarrow 2NH_3 + CO_2,$$

$$NH_3 + H_2O \rightarrow NH_4^+ + OH^-,$$

$$CO_2 + H_2O \rightarrow CO_3^{2-} + 2H^+,$$

$$Co^{+2} + xCO_3^{2-} + yOH^- + H_2O \rightarrow Co(CO_3)_x(OH)_y \cdot H_2O,$$

$$Co(CO_3)_x(OH)_y \cdot H_2O \xrightarrow{\Delta} Co_3O_4 + xCO_2 + yH_2O.$$

3.2. Material characterization for structural analysis

The phase purity and crystallinity of pristine Co_3O_4 and Ir_{SAC}–Co_3O_4 samples were confirmed by XRD analysis. The distinct and prominent diffraction peaks for both samples (Fig. S1) are consistent with the cubic phase of Co_3O_4 (JCPDS 00-042-1467) with cell parameters $a = b = c = 8.07$ Å and $\alpha = \beta = \gamma = 90°$. The well-matched diffraction patterns indicate the formation of a pure phase in the synthesized samples. A broad peak at 25° is observed corresponding to the CC. The diffraction angles of the Ir_{SAC}–Co_3O_4 sample show no significant change or shift, suggesting that Ir single atoms are not altering the lattice parameters and crystal structure of Co_3O_4. Moreover, no diffraction peaks for Ir and IrO_2 are observed in the Ir_{SAC}–Co_3O_4 sample, indicating the absence of both metallic Ir and IrO_2.

The morphology of both pristine Co_3O_4 and Ir_{SAC}–Co_3O_4 samples was analyzed by FESEM. The FESEM images of the pristine sample at various resolutions are shown in Fig. S2a and b that reveal the uniformly distributed nanoflower morphology throughout the carbon cloth. The synthesized nanoflower is composed of thin nanorods of thickness ranging from 100 to 400 nm along with rough morphology. Fig. 1a and b show the FESEM images of the Ir single atom-doped Co_3O_4 sample at low and high resolutions, confirming the retention of morphology. Thus, the uniform distribution of nanoflowers along with a rough surface ensures the complete exposure of catalytic sites and efficient contact between the electrode and the electrolyte. The FESEM images of other samples synthesized using various concentrations of the $IrCl_3$ solution are given in Fig. S2(c–h). The morphology of all the samples remained similar across

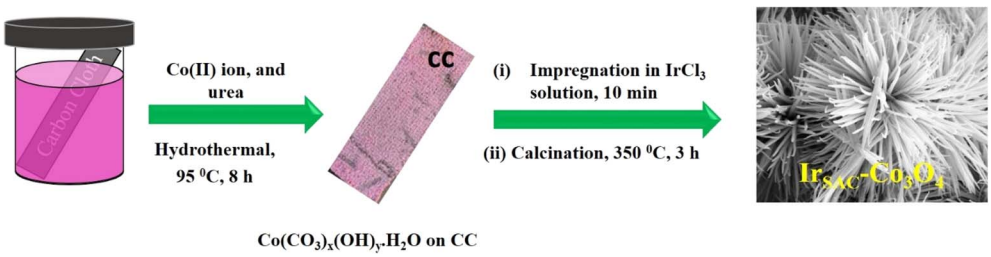

Scheme 1 Schematic of the synthesis of Ir_{SAC}–Co_3O_4 on CC.

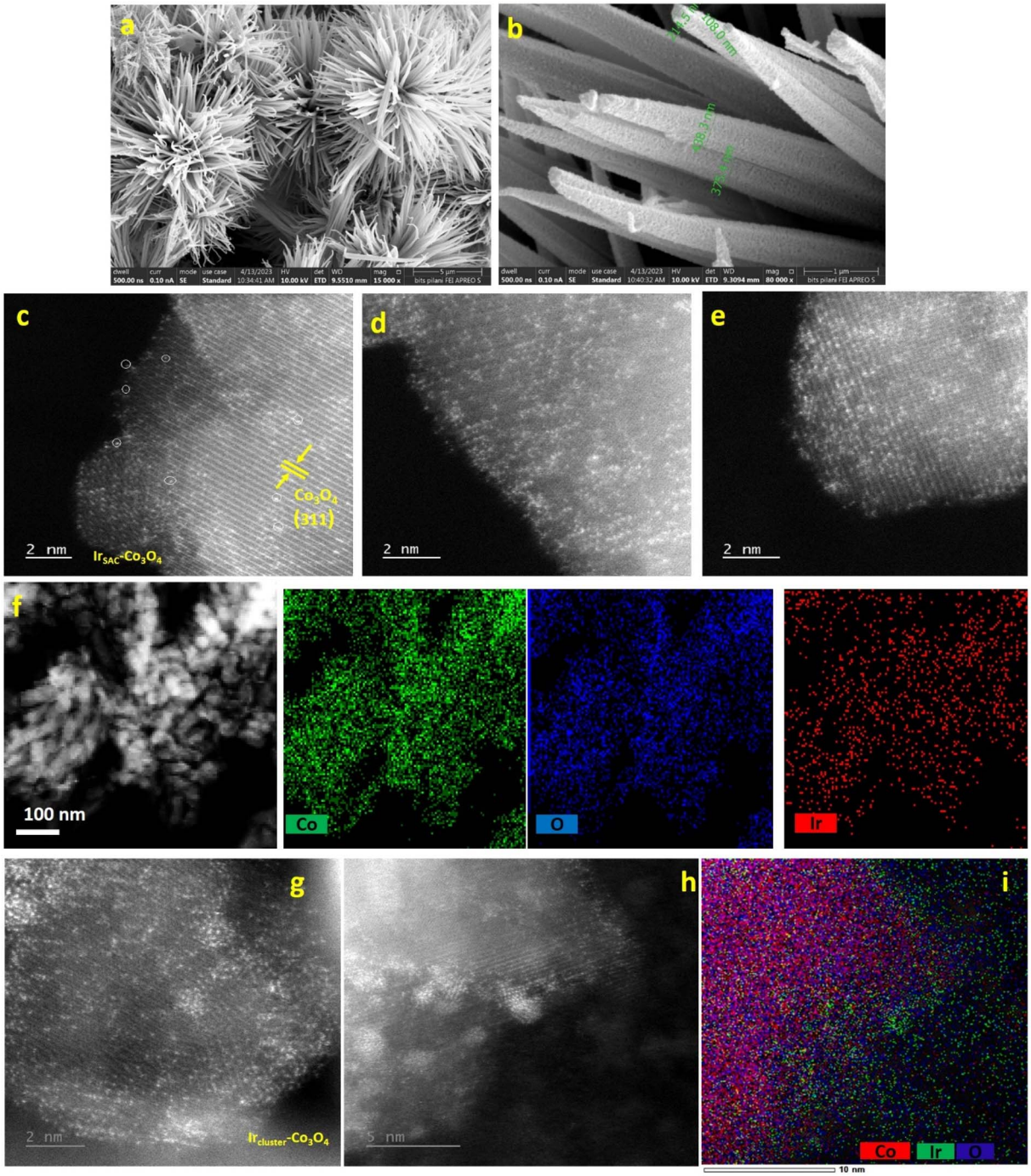

Fig. 1 FESEM images at low (a) and high (b) resolutions, HAADF-STEM images with the optimized Ir concentration of 10 mg mL^{-1} (c)–(e), and the corresponding STEM elemental mapping images (f) of Ir_{SAC}–Co_3O_4. HAADF-STEM images with the Ir concentration of 25 mg mL^{-1} (g) and (h) and elemental mapping image of the $Ir_{cluster}$–Co_3O_4 (i).

varying concentrations of the $IrCl_3$ solution. This indicates that the amount of $IrCl_3$ does not influence the morphology of the material. The SEM-EDS mapping analysis of Ir/Co_3O_4 samples with varying Ir concentrations is presented in Table S2. The results indicate the uniform distribution of Ir elements with the increased concentration.

To further confirm the morphology and crystallinity of pristine Co_3O_4 and Ir_{SAC}–Co_3O_4, TEM and HRTEM analyses were performed. The TEM image of Co_3O_4 (Fig. S3a and b) verifies the nanoflower morphology. The *d*-spacing value of the (311) plane was calculated to be 0.24 nm for the pristine Co_3O_4 sample (Fig. S3c). The TEM image (Fig. S3d and e) of the Ir single-atom-doped sample shows a similar morphology of nanoflowers made of nanorods. The atomic dispersion of Ir single atoms over a Co_3O_4 support was confirmed by the HAADF-STEM images. As shown in Fig. 1c–e, the isolated bright

spots corresponding to Ir atoms are uniformly distributed across the entire Co_3O_4 support matrix, showing the successful synthesis of Ir single atoms without any aggregation. HAADF-STEM element mapping analysis (Fig. 1f) further validates the uniform atomic distribution of Ir single atoms over the CO_3O_4 surface. Additionally, HAADF-STEM analysis of the Ir/Co_3O_4 sample with the highest content (4.91 wt%) of Ir was performed. Fig. 1g and h show the bright spots in aggregate form, indicating the formation of an Ir cluster on the Co_3O_4 support ($Ir_{cluster}$–Co_3O_4). The aggregated form of Ir cluster was further verified by EDS mapping analysis (Fig. 1i). This observation demonstrates the transition from atomically dispersed Ir to aggregation in a cluster form with the increasing content (wt%) of Ir.

In order to gain insights into the valence state and local coordination environment, the X-ray near-edge fine structure (XANES) and extended X-ray absorption fine structure (EXAFS) spectra were recorded for the Ir_{SAC}–Co_3O_4 sample, for which commercial IrO_2 and Ir foil were used as benchmarks. Fig. 2a shows the normalized XANES spectrum at the Ir L_3-edge for Ir_{SAC}–Co_3O_4 along with IrO_2 and Ir foil for reference. The intensity of the white line/spectral line intensity (H_A) of the Ir L_3-edge spectrum represents the density of the unoccupied Ir-d orbitals and the extent of surface chemisorption of oxygen.[39,40] Remarkably, the high intensity of the white line for Ir_{SAC}–Co_3O_4 compared to Ir foil indicates the increased density of unoccupied orbitals of Ir atoms.[41] This explains the superior performance of Ir_{SAC}–Co_3O_4 for the electrocatalytic OER, since an increased density of unoccupied orbitals promotes the

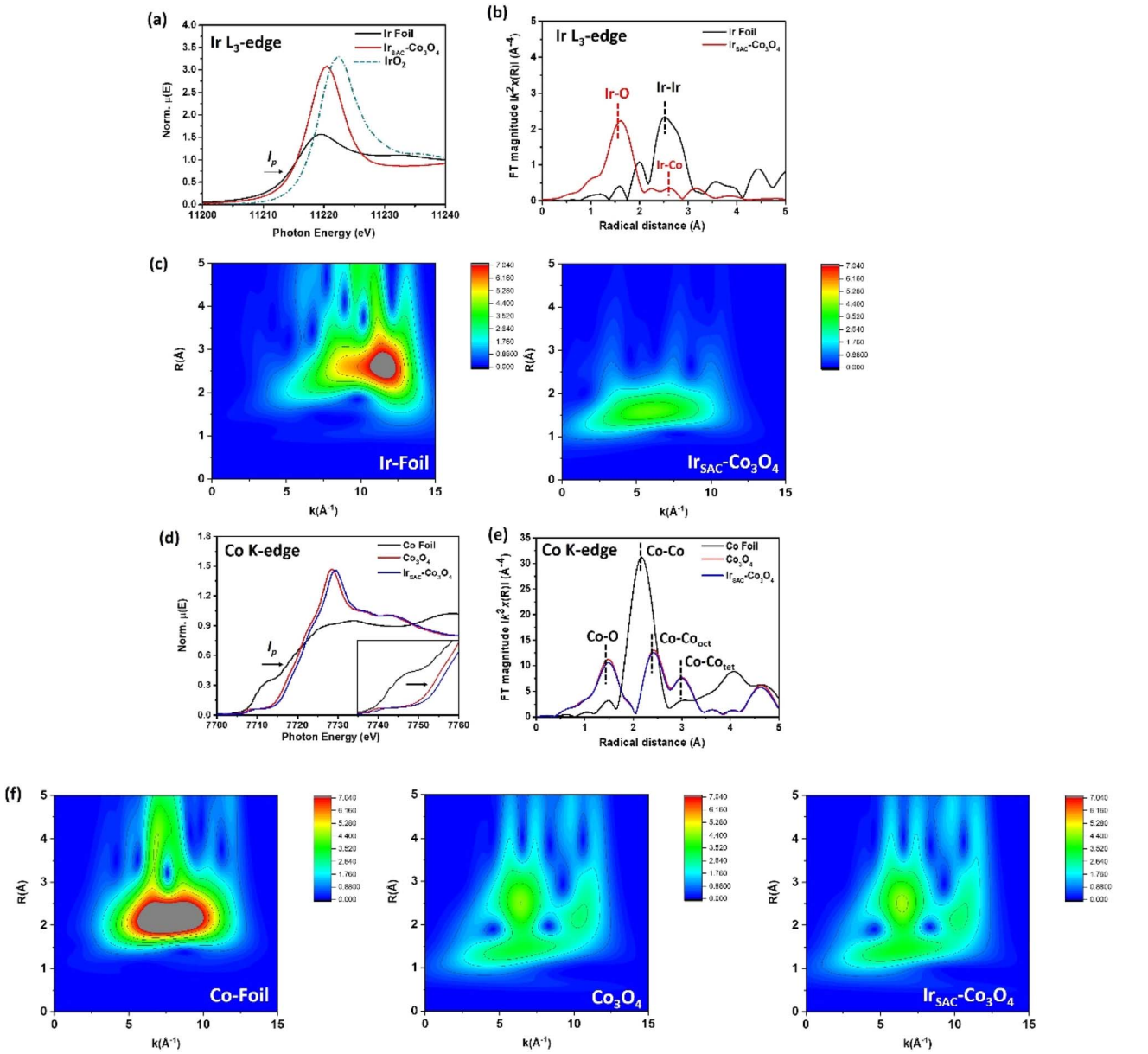

Fig. 2 X-ray absorption spectroscopy. (a) XANES and (b) FT-EXAFS spectra and (c) WT patterns at the Ir L_3-edge for Ir_{SAC}–Co_3O_4 along with the reference samples. (d) XANES and (e) FT-EXAFS spectra and (f) WT patterns at the Co K-edge for Ir_{SAC}–Co_3O_4 and the reference samples.

electrocatalytic efficiency. Furthermore, the shift in the inflection point (I_P) indicates the higher threshold energy (E_0) of Ir_{SAC}–Co_3O_4 than that of the Ir-foil, which validates the depletion of the Ir-d band. The higher surface oxygen chemisorption and depletion of the d-band of Ir present in the Ir_{SAC}–Co_3O_4 sample further suggest the existence of Ir single atoms.[42] Additionally, the position of the inflection point (I_P) of Ir_{SAC}–Co_3O_4 lies between the Ir foil and IrO_2, which indicates the partial oxidation of Ir atoms in the Ir_{SAC}–Co_3O_4 sample. The bonding of Ir single atoms with the Co and O atoms of the support matrix can be attributed to the positive shift in the threshold energy (E_0) and the partial oxidation state of Ir atoms in Ir_{SAC}–Co_3O_4.

The Fourier transform EXAFS (FT-EXAFS) spectra of Ir_{SAC}–Co_3O_4, along with the reference sample (Ir foil and IrO_2) at the Ir L_3-edge, are shown in Fig. 2b. The related parameters for the quantitative structure of both Co_3O_4 and Ir_{SAC}–Co_3O_4 are summarized in Table S3. As evident, the Ir–Ir scattering path appears at 2.51 Å, corresponding to the Ir foil. For the Ir_{SAC}–Co_3O_4 sample, the peak corresponding to the Ir–Ir scattering is absent, and also the zero-coordination number (CN) for Ir–Ir bond pair (Table S3) firmly substantiates the formation of Ir single atoms on the Co_3O_4 support. The peak across 1.0 to 3.0 Å corresponds to the Ir–O and Ir–Co bond pairs with $CN_{Ir-O} = 3.01$ and $CN_{Ir-Co} = 2.16$, respectively. The reduced coordination of 3.01 for the Ir–O bond, in contrast to the expected CN = 6 for standard IrO_2, further validates the partial oxidation of Ir single atoms. Wavelet transform (WT) analysis provides additional insights into the structural characteristics. As illustrated in Fig. 2c, the Ir_{SAC}–Co_3O_4 catalyst does not show the peak corresponding to the Ir–Ir bond pair, further strengthening the presence of Ir-single atoms.

The chemical state of Co was also investigated by Co k-edge XAS analysis. The XANES spectra of Ir–Co_3O_4, pristine Co_3O_4, along with the Co foil, are shown in Fig. 2d, which includes essential characteristics such as inflection point (I_P). The positive shift in the inflection point (I_P) for Ir_{SAC}–Co_3O_4 compared to the pristine Co_3O_4 suggests a higher valence state of Co, ascribed to the electron transfer from Co to Ir through Ir–Co bonding. Furthermore, the FT-EXAFS spectrum reveals the coordination environment of Co-atoms. As shown in Fig. 2e, both Ir_{SAC}–Co_3O_4 and Co_3O_4 show similar FT-EXAFS profiles, indicating that the Ir single atoms do not affect the local structure of the Co_3O_4 lattice. Furthermore, the WT pattern of both Co_3O_4 and Ir_{SAC}–Co_3O_4 exhibits a missing peak intensity at 2.01 Å, which belongs to the Co–Co bond pair in the Co foil, indicating the total oxidation of Co atoms in both samples (Fig. 2f). The overlay spectra of Ir–Co_3O_4 EXAFS and corresponding fitting are given in Fig. S4a.

XPS analysis was performed to further assess the valence and chemical states of all elements in both the Co_3O_4 and Ir_{SAC}–Co_3O_4 samples. Fig. S4b–d demonstrate the survey and deconvoluted spectra of Co 2p and O 1s, respectively, for the pristine Co_3O_4 sample.

The deconvoluted XPS spectra of Co 2p exhibit two doublets along with three satellite peaks (Fig. S4c). The binding energy (BE) value of the doublets corresponding to the Co $2p_{3/2}$ spectra is 779.37 and 780.81 eV, indicating the presence of Co^{3+} and Co^{2+}, respectively. Another doublet peak for the Co $2p_{1/2}$ state appeared at 794.31 and 795.75 eV, corresponding to Co^{3+} and Co^{2+}, respectively. Three peaks can be seen in the O 1s deconvoluted XPS spectra (Fig. S4d): O1 (positioned at 529.52 eV), O2 (530.90 eV), and O3 (532.24 eV). The metal–oxygen bond or lattice oxygen is attributed to the peak at O1. The peak at O2 associated with the O-vacancy, while the peak at O3 corresponds to the oxygen in absorbed water. All of the BE values of Co and O are well matched with the literature.[43,44]

Moreover, the presence of Ir and other ions in the Ir_{SAC}–Co_3O_4 sample was verified further with XPS survey scan (Fig. 3a). The deconvoluted Co 2p spectra reveal two prominent groups of spin–orbit coupling peaks (Fig. 3b). The peaks at 779.98 and 795.07 eV represent the Co^{3+} ions in the Co $2p_{3/2}$ and Co $2p_{1/2}$ states, respectively. Other two pairs of Co^{2+} are located at 781.40 and 796.68 eV, corresponding to Co $2p_{3/2}$ and Co $2p_{1/2}$. A substantial electronic interaction between the Ir single atoms and the support atoms is shown by the binding energy values of Co 2p in Ir_{SAC}–Co_3O_4, which exhibit a positive shift of approximately 0.63 eV compared to the pure sample. The three satellite peaks are positioned at 784.82 and 788.93 eV, corresponding to Co^{2+} and Co^{3+} for the Co $2p_{3/2}$ shake-up satellite, respectively, while another peak at 804.41 eV corresponds to the shake-up satellite peak of Co^{3+} for Co $2p_{1/2}$. The XPS spectra of O 1s are deconvoluted into three peaks (Fig. 3c). The peak at 531.53 eV (O2) is attributed to oxygen vacancies, while the peaks at 530.28 eV and 532.48 eV correspond to lattice oxygen (M–O) and adsorbed water (O–H_2O), respectively. The binding energy value of O 1s exhibits a positive shift of approximately 0.7 eV compared with the pure Co_3O_4, indicating a significant surface oxygen chemisorption following the insertion of an Ir single atom. The O-vacancy was quantified, which shows the % O-vacancy in Co_3O_4 and IrSAC-Co_3O_4 are 32.6 and 23.26, respectively. All the binding energy values for Co_3O_4 and Ir_{SAC}–Co_3O_4 are listed in Table S4.

The XPS spectra of Ir 4f is deconvoluted into three peaks (Fig. 3d). The peaks positioned at 62.39, 65.19, and 66.94 eV correspond to Ir $4f_{7/2}$, Ir $4f_{5/2}$, and satellite peak, respectively. Furthermore, a peak appeared at 60.32 eV, corresponding to Co 3p. A higher binding energy of Ir single atoms in the Ir_{SAC}–Co_3O_4 sample than that of the metallic Ir (60.8 eV) indicates that Ir atoms are highly oxidized, which aligns well with the Ir L_3-edge XANES result. Biswal and co-workers[45] observed that the values of binding energies of Ir $4f_{7/2}$ in IrO_2 and $IrCl_3$ are 62.54 and 62.13 eV, respectively. The observed binding energy value (62.39 eV) of Ir $4f_{7/2}$ for the Ir_{SAC}–Co_3O_4 sample falls between the binding energy values for metallic Ir (60.8 eV) and IrO_2 (62.54 eV), indicating the intermediate oxidation state of Ir single atoms that align well with the Ir L_3-edge XANES findings.

The enhanced valence state of the Co atoms of the substrate could be attributed to the highly oxidized Ir atoms over Co_3O_4, which acts as a Lewis acid and pulls the electron from the nearby Co atoms. By calculating the area within the curve, the ratio of Co^{2+}/Co^{3+} is calculated for both Co_3O_4 and Ir_{SAC}–Co_3O_4, to confirm the electron-withdrawing nature of Ir atoms. The value of the $Co^{2+/}Co^{3+}$ ratio for the Co_3O_4 sample is 0.43. Furthermore, the ratio in the Ir_{SAC}–Co_3O_4 sample is 0.39. The higher valence state of Co for Co_3O_4 is suggested by this lower value of the $Co^{2+/}Co^{3+}$ ratio, which further indicates

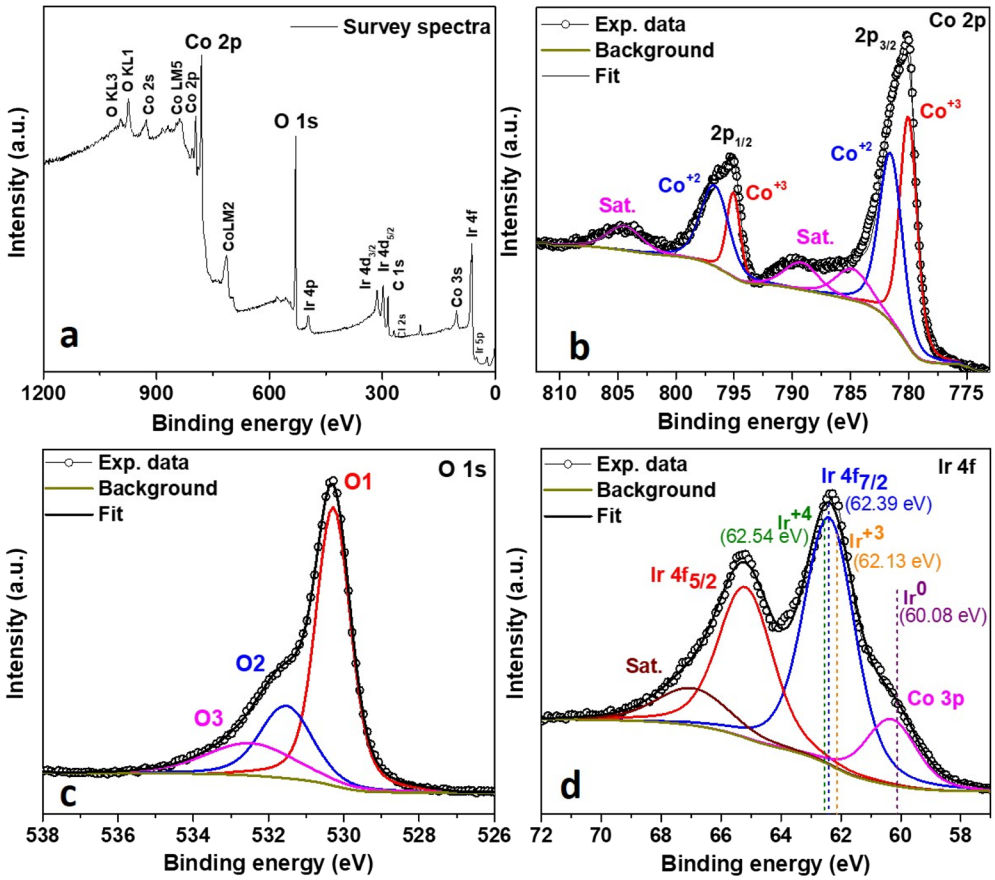

Fig. 3 XPS analyses of the Ir_{SAC}–Co_3O_4 sample: (a) survey spectrum and deconvoluted XPS spectra of (b) Co 2p, (c) O 1s, and (d) Ir 4f regions.

a significant electronic interaction between the Co atoms and the single Ir atoms that results in electron relocation. The Co K-edge XANES study and the XPS analysis results are in good agreement. Strong electronic coupling between the single atom and the support matrix is thus represented by the positive shift in the binding energy values of both Co and oxygen as well as the enhanced valence state of Co in Ir_{SAC}–Co_3O_4 in comparison to the pristine Co_3O_4. Our group noticed a similar phenomenon of decreased Ni^{2+}/Ni^{3+} ratio following heteroatom doping.[46]

The formation of oxygen vacancy was further verified by electron paramagnetic resonance (EPR) analysis. Both pristine Co_3O_4 and Ir_{SAC}–Co_3O_4 samples exhibit clear signals in the EPR spectra (Fig. S5), indicating the presence of unpaired electrons associated with oxygen vacancies. The measured g values (spectral splitting factor) are 1.91 and 1.93 for pristine Co_3O_4 and Ir_{SAC}–Co_3O_4, respectively. The coordination of Ir single atoms with O regulates the oxidation state and basic catalytic properties of single-atom catalysts, while the bonding of Ir with the Co atoms of the support matrix gives stability to the single atoms, which is reflecting in the durability during the electrocatalytic OER.[28]

4. Electrocatalytic performance: OER study

The electrocatalytic activity of all the developed samples was assessed in 1 M KOH, using a three-electrode setup. The LSV analysis was performed at a scan rate of 2 mV s^{-1}. The OER performance of pristine Co_3O_4 and IrO_2 supported on CC was evaluated for comparison. The LSV polarization curve (Fig. 4a) shows that Ir_{SAC}–Co_3O_4 exhibited enhanced OER activity, requiring a low overpotential (η) of only 270 mV to reach a current density of 10 mA cm^{-2}, which significantly outperformed the benchmark IrO_2 catalyst (η_{10} = 410 mV) and pristine Co_3O_4 (η_{10} = 350 mV). The substantially improved OER activity of Ir_{SAC}–Co_3O_4 can be attributed to the presence of Ir single atoms over the Co_3O_4 support. The enhanced activity of Ir_{SAC}–Co_3O_4 can be seen by a histogram (Fig. 4b) that is plotted at 1.60 V *vs.* RHE for Ir_{SAC}–Co_3O_4, Co_3O_4 and IrO_2.

To optimize the amount of Ir, other samples were prepared using different concentrations of $IrCl_3$ xH_2O. The onset potential to achieve 10 mA cm^{-2} current density is lowest for the catalyst prepared by using 10 mg mL^{-1} concentration of Ir (Ir_{SAC}–Co_3O_4) and highest for the sample synthesized by using 25 mg mL^{-1} concentration of Ir ($Ir_{cluster}$–Co_3O_4) (Fig. S6). This result reveals that, despite the $Ir_{cluster}$–Co_3O_4 sample having a higher Ir loading of 4.91 wt%, its OER activity is inferior compared to the Ir_{SAC}–Co_3O_4 sample, which contains a lower Ir content of 3.02 wt%. The superior performance of Ir_{SAC}–Co_3O_4 demonstrates the high atom utilization efficiency of SACs, where atomically dispersed Ir atoms are more effectively involved in the catalytic process, resulting in a higher catalytic activity than that of the higher Ir loading in the cluster-based counterpart.

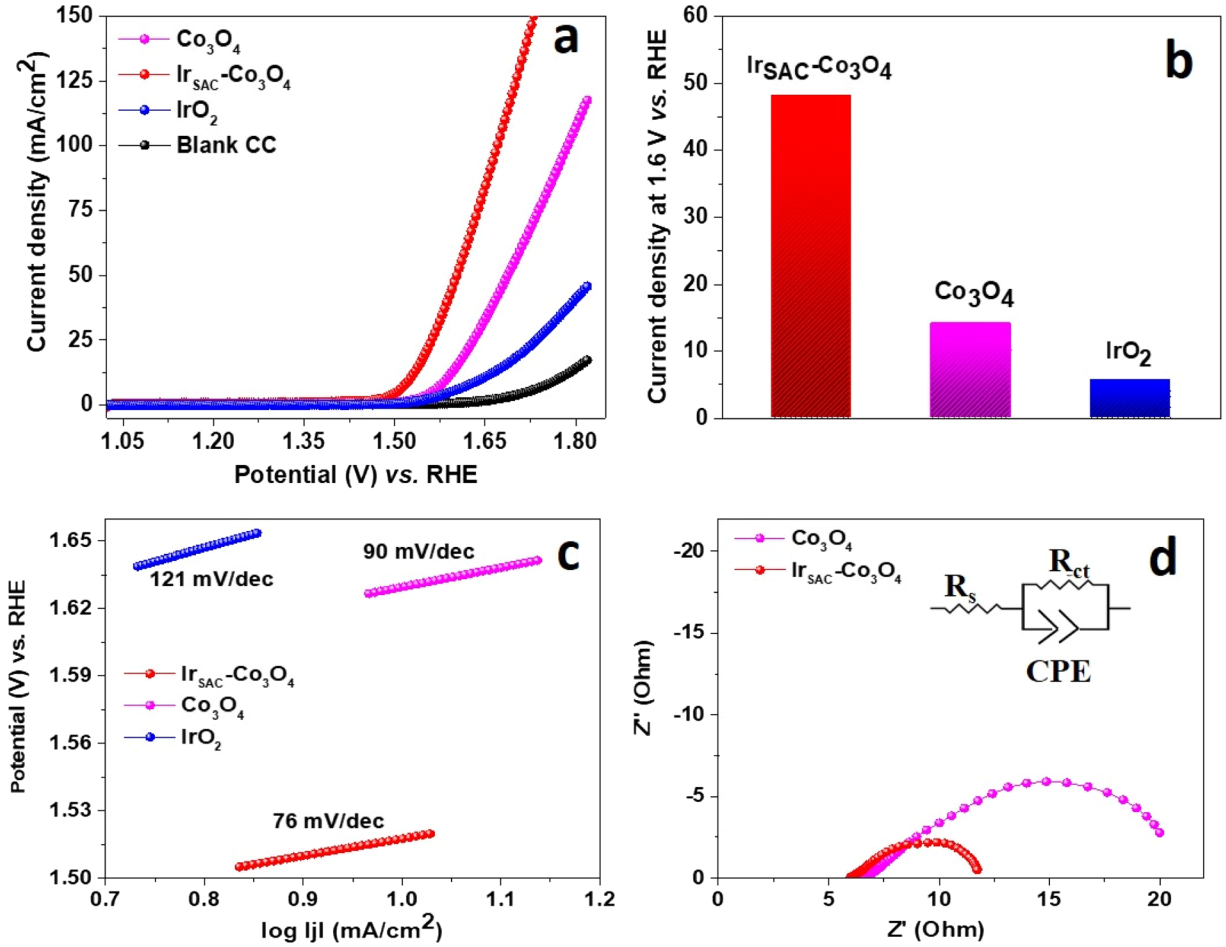

Fig. 4 Electrocatalytic OER activity: (a) LSV polarization curve for blank CC, Co_3O_4, Ir_{SAC}–Co_3O_4, and IrO_2 for the OER, (b) histogram plot at 1.6 V *vs.* RHE, (c) Tafel plots of Co_3O_4, Ir_{SAC}–Co_3O_4, and IrO_2, and (d) Nyquist plots of the pristine Co_3O_4 and Ir_{SAC}–Co_3O_4.

The optimized concentration was further confirmed by TOF and mass activity analysis (Table S5). A comparative analysis of OER values reported in the literature is provided in Table S6. The high valence state of Ir atoms arising from the robust electronic interaction from the support matrix, which exhibited an elevated density of unoccupied orbitals, also enhanced the valence state of Co atoms, together contributing to the improved OER activity of Ir_{SAC}–Co_3O_4. Moreover, the superior OER performance of Ir_{SAC}–Co_3O_4 was corroborated by its higher mass activity, at a fixed potential of 1.55 V *vs.* RHE. The values of mass activity for Ir_{SAC}–Co_3O_4, Co_3O_4 and IrO_2 are 274.28, 35.74, and 35.71 A g^{-1}, respectively. Compared to pristine Co_3O_4, Ir_{SAC}–Co_3O_4 exhibits 8 times greater mass activity, indicating a significant electron transfer efficiency, as evidenced by its electrocatalytic activity.

In order to assess the kinetics of the electrode material, the Tafel slope was evaluated using the Tafel equation (given in the SI). The superior reaction kinetics of Ir_{SAC}–Co_3O_4 was reflected by its significantly smaller Tafel slope value (76 mV dec^{-1}) in contrast to Co_3O_4 (90 mV dec^{-1}) and IrO_2 (121 mV dec^{-1}) (Fig. 4c). The faster charge transfer kinetics of Ir_{SAC}–Co_3O_4 was further assessed by the EIS analysis (Table S7). Fig. 4d shows the lower charge transfer resistance (R_{CT}) for the Ir single-atom-doped sample (5.12 Ω) compared with the pristine Co_3O_4 (12.19 Ω). The lower R_{CT} value of Ir_{SAC}–Co_3O_4 indicates improved kinetics and higher charge transfer efficiency at the electrode–electrolyte interface of the material compared to the pristine Co_3O_4. Furthermore, the lower charge transfer resistance of Ir_{SAC}–Co_3O_4 unveils the close proximity between the electrode and the electrolyte. An equivalent circuit with solution resistance (R_S), charge transfer resistance (R_{CT}), and a constant phase element (CPE) is shown in the inset of Fig. 4d. To further corroborate the enhanced intrinsic activity of Ir_{SAC}–Co_3O_4 for the OER, reflected by its lower overpotential and higher mass activity than those of the pristine Co_3O_4 and benchmark IrO_2, the TOF was calculated. The obtained TOF values at an overpotential of 370 mV for Ir_{SAC}–Co_3O_4, Co_3O_4, and IrO_2 are 0.03, 0.005, and 0.002 s^{-1}. The TOF value of Ir_{SAC}–Co_3O_4 is 6 times higher than that of pristine Co_3O_4 and 15 times higher than that of the benchmark IrO_2. The significantly higher TOF value of Ir_{SAC}–Co_3O_4 than that of both pristine Co_3O_4 and IrO_2 indicates its enhanced intrinsic activity for the OER. Table S8 contains a list of all the recorded values of both Co_3O_4 and Ir_{SAC}–Co_3O_4 samples.

Moreover, to calculate the electrochemical active surface area (ECSA), first the electric double layer capacitance (C_{dl}) was evaluated by measuring the CV curves in the non-faradic potential region (Fig. S7a and b). The double-layer charging current was plotted against the scan rate for both pristine Co_3O_4 and Ir_{SAC}–Co_3O_4 samples at a potential of 1.11 V *vs.* RHE (Fig. S7c). The calculated ECSA values are 12.63 cm^2 and 4.03 cm^2 with a roughness factor of 78.75 and 25.18 for Ir_{SAC}–Co_3O_4 and Co_3O_4, respectively. The increased values of ECSA and roughness factor indicate the elevation in the catalytic active sites and better interaction of reactants with the electrode after the Ir single atom insertion to the Co_3O_4 support.

To comprehend the increased activity of Ir_{SAC}–Co_3O_4, CV analysis was performed for evaluation (Fig. S8). The CV curve can be separated into three different regions. Region (a) signifies the adsorption of OH^- ions to the active site. Region (b) contains the oxidation of Co^{2+} to Co^{3+} and the generation of O*, a crucial intermediate that binds with the OH^- group to produce *OOH for oxygen evolution. Finally, the higher potential region (c) consists of the formation of O_2 *via* the coupling of O–O. The significant decrease in both the peak potential and peak area for Co^{2+}/Co^{3+} in the Ir_{SAC}–Co_3O_4 sample related to Co_3O_4 shows the modified electronic structure of the Co_3O_4 support as a result of strong electronic coupling with Ir single atoms. This electronic coupling accelerates the formation of Co^{2+} to Co^{3+} and the possible surface reconstruction from Co_3O_4 to the active CoOOH phase, and thus promotes the OER kinetics by elevating the pre-oxidation process.[35,47,48] Lin and co-workers[49] identified a similar phenomenon of the conversion of Ni^{2+} to Ni^{3+} during the electrocatalytic OER, which was accelerated by the presence of Pt single atoms. Moreover, with the help of *in situ* XAS analysis, Li and co-workers[50] reported the elevated oxidation states of Co and Fe during the OER process.

The durability of Ir_{SAC}–Co_3O_4 in the OER was assessed by 1000 LSV cycles along with the chronoamperometry test. No significant change was observed in the LSV after 1000 cycles (Fig. 5a). Furthermore, chronoamperometry analysis performed at 1.54 V *vs.* RHE shows no evident degradation after 96 h (Fig. 5b). Additionally, the durability of the catalyst was further evaluated at a higher current density of 130 mA cm^{-2} under a fixed potential of 1.77 V. As shown in Fig. 5c, no significant current degradation was observed even after long operational hours, confirming the superior durability of the catalyst at elevated current density and highlighting its potential for industrial applications. This long-term durability further validates the robust electronic interaction of the Co_3O_4 support and Ir single atoms, which restrains the aggregation of Ir single atoms throughout the electrocatalysis process. In this regard, He and co-workers reported an extended durability of Ir single atoms anchored on $Ni(OH)_2$, which is due to the strong electronic interaction between the Ir single atoms and the support matrix.[51] For the post-electrocatalysis characterizations, FESEM and XPS analyses were performed for Ir_{SAC}–Co_3O_4. The nanoflower-like morphology of Ir_{SAC}–Co_3O_4 was retained (Fig. S9). Moreover, XPS analysis was performed to determine the chemical and electronic states of elements after electrocatalysis. The presence of all elements was confirmed by the XPS survey spectra (Fig. S10a). The high-resolution XPS spectrum of Co 2p (Fig. S10c) reveals two doublets and three satellite peaks. The binding energy value of Co $2p_{3/2}$ remains constant with peaks at 780.04 and 781.27 eV, and for Co $2p_{1/2}$, peaks appeared at 795.06 and 796.44 eV. Moreover, the O 1s binding energy remains constant and appears at 530.22, 531.69, and 533.23 eV (Fig. S10b). The binding energy for Ir also stays the same and appears at 62.31 and 60.44 eV for $4f_{7/2}$ and $4f_{5/2}$, respectively (Fig. 5d). The post-XPS analysis shows that the electronic state of both Co and Ir remains unchanged after the 96 h stability test, which represents the superior robustness of the Ir single atoms on the Co_3O_4 support. To further confirm the firmness of the Ir single atoms on Co_3O_4, ICP-OES analysis of the electrolyte was performed after 24 h of electrocatalysis. The amount of Ir in the electrolyte was insignificant, which indicates no leaching of the Ir atom during catalysis. Moreover, following a 24 h stability test (chronoamperometry analysis), the UV-vis spectrum (Fig. 5e) of the electrolyte exhibits no absorption peak, compared to the UV-vis spectrum of the $IrCl_3$ solution. The presence of two prominent peaks at 375 and 412 nm corresponds to the hydrated Ir^{3+} ions in the $IrCl_3$ solution. A digital image of the electrolyte after electrocatalysis (inset of Fig. 5e) shows a colorless solution, suggesting no catalyst leaching. Furthermore, post-electrocatalysis HAADF-STEM analysis was performed to ensure the stability of Ir single atoms on the support. The bright, isolated spots corresponding to the Ir single atoms uniformly dispersed across the support matrix (Fig. 5f and g) show that there is no aggregation of Ir single atoms during the electrocatalysis.

To further gain insights into the possible changes in the catalyst surface after electrocatalysis, HRTEM and FFT analyses were performed following 27 h of chronoamperometry. The post-electrocatalysis HRTEM image (Fig. 5h) demonstrates that the sample maintains its highly crystalline lattice fringes for the cubic Co_3O_4 phase. However, we also observed the presence of a surface reconstructed layer that shows lower crystallinity as compared to the Co_3O_4 phase. This region corresponds to the formation of the CoOOH active phase during the electrocatalysis. The associated FFT images corresponding to this reconstructed surface region exhibit diffuse diffraction spots that match with the hexagonal symmetry of the CoOOH (Fig. 5i). Meanwhile, the FFT pattern of the crystalline region exhibits distinct cubic diffraction spots (Fig. 5j), consistent with spinel Co_3O_4. These findings confirm that during the electrocatalytic OER, the oxide surface reconstructed into the highly active oxyhydroxide phase. The phenomenon of surface reconstruction confirmed from HRTEM analysis is well reported in the literature. Li and co-workers reported similar surface reconstruction of Co–Cr spinel oxides to the CoOOH phase. The surface reconstruction and formation of CoOOH was identified by the post electrocatalysis HRTEM images, where the poor crystalline region emerges due to the formation of an active oxyhydroxide phase during the OER.[32] Zou and co-workers also reported a similar structural evolution of Co_3O_4 to cobalt oxyhydroxide (CoOOH) during the OER in 1 M KOH. The presence of CoOOH was validated by the post electrocatalysis HRTEM analysis. The reconstructed surface shows a clear boundary

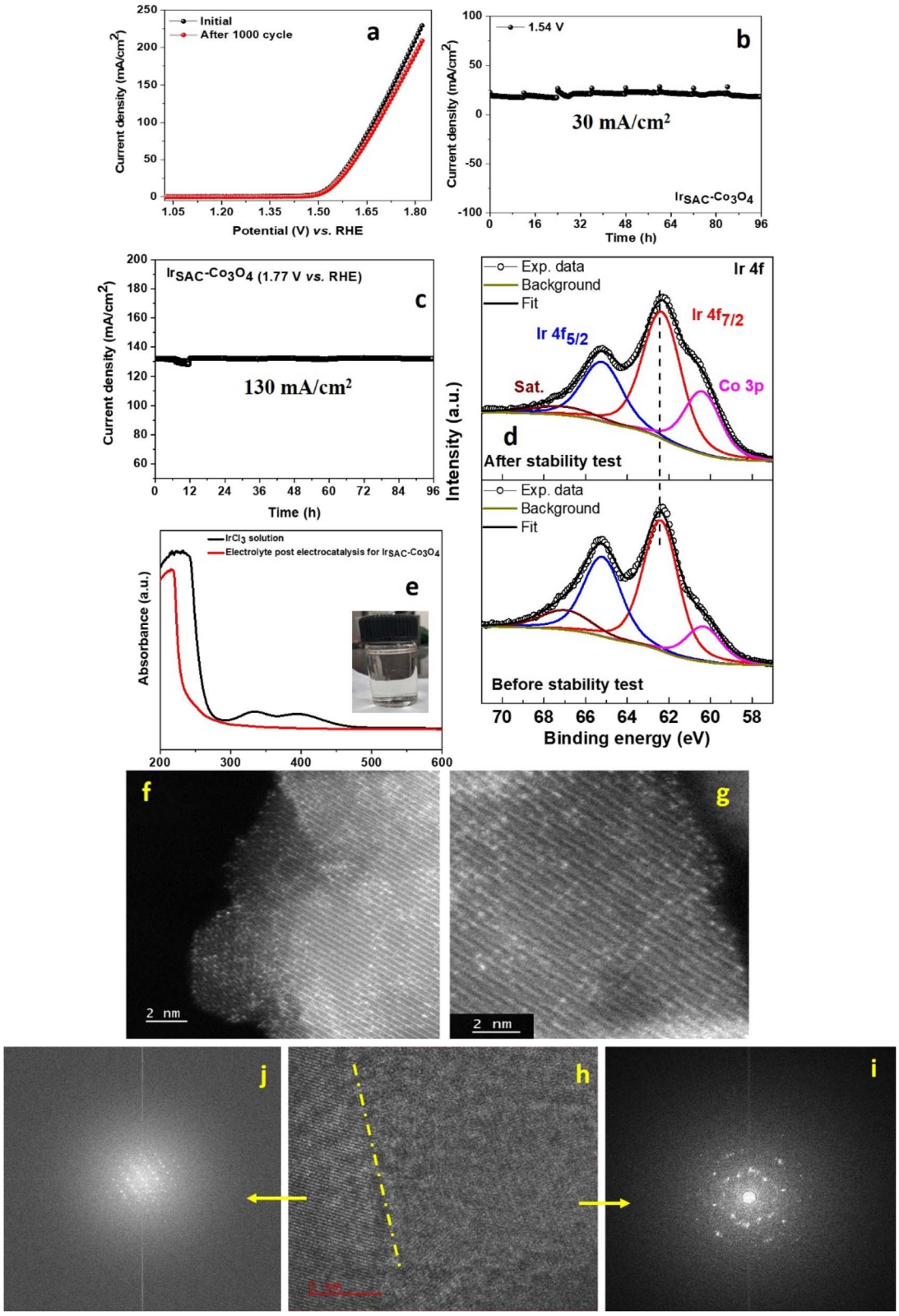

Fig. 5 (a) LSV polarization curve before and after 1000 cycles. Chronoamperometry analysis for long-term stability at (b) 1.54 V *vs.* RHE and (c) 1.77 V *vs.* RHE. (d) XPS spectra of Ir 4f before and after the stability test for Ir_{SAC}–Co_3O_4. (e) UV spectra of Ir_{SAC}–Co_3O_4 after 24 h of electrocatalysis. (f) and (g) Post-electrocatalysis HAADF-STEM images of Ir_{SAC}–Co_3O_4. (h) HRTEM image of Ir_{SAC}–Co_3O_4 after post-electrocatalysis, showing a distinct boundary between the highly crystalline Co_3O_4 core and a surface-reconstructed, low-crystallinity CoOOH layer. Corresponding FFT images of (i) hexagonal symmetry for low-crystalline CoOOH phase and (j) cubic symmetry corresponding to Co_3O_4.

between the crystalline Co_3O_4 core and the CoOOH shell with different crystallinities.[33] Mori and co-workers found the amorphous reconstructed layer with the help of both HRTEM and corresponding FFT images.[52] Along with post-electrocatalysis HRTEM analysis, Raman analysis of the Ir_{SAC}–Co_3O_4 sample after 24 and 48 h (chronoamperometry) was performed to further verify the surface reconstruction. The Ir_{SAC}–Co_3O_4 sample exhibits the characteristic Raman peaks (Fig. S11) at ~677, 608, 512, 189 and 471 cm^{-1}, associated with A_{1g}, three F_{2g} and E_g phonon modes of Co_3O_4, respectively. The A_{1g} and F_{2g} band can be related to the Co^{3+}-O and Co^{2+}–O bonds, respectively.[53] The Raman spectra of the post-electrocatalytic sample exhibit a significant red shift in the peak positions. This shift signifies the weakening of Co–O bonds, the formation of oxygen vacancies, and surface reconstruction.[54,55] Huang and co-workers reported a similar red shift to the Raman peak positions for Co_3O_4/CeO_2 after the OER. The shift was further attributed to the change in the local bonding environments due to surface reconstruction.[56] Post-electrocatalysis XRD analysis (Fig. S12) shows clear and prominent peaks, which are well matched with Co_3O_4 (JCPDS 00-042-1467). The well-matched 2θ values show that there is no change in the crystal structure of the sample. Therefore, all these analyses strengthen the robust electronic interaction and durability of Ir single atoms on the Co_3O_4 support matrix.

5. First-principles DFT calculations

5.1. Crystal structures of Co_3O_4 and Ir_{SAC}–Co_3O_4 systems

Under ambient pressure (P = 0 GPa), the Co_3O_4 compound exhibits a spinel crystal structure and belongs to the face-centered cubic symmetry with the space group $Fd\bar{3}m$ and space group number 227. The unit cell of the crystal consists of two non-equivalent Co ions with varying valence configurations, namely, Co^{3+} and Co^{2+}. While the four O atoms in the unit cell form several tetrahedral environments by surrounding each Co^{2+} ion, the Co^{3+} ion is enclosed by six O atoms in order to form an octahedral coordination. The optimized crystal structure of Co_3O_4, so attained from the DFT calculations, is shown in Fig. 6a. The associated optimized lattice parameter of the system is estimated to be ~8.046 Å, which is found to match closely with our XRD result (*vide supra*) and other results reported elsewhere in the literature.[57,58]

To model the Ir_{SAC}–Co_3O_4 compound, a Co atom has been substituted by a single Ir atom on the Co_3O_4 crystal. The substitutional site for Ir in the Co_3O_4 lattice was selected based on the local coordination environment, guided by experimental XAS analyses. Specifically, the coordination number (CN) between Ir and surrounding oxygen atoms has been considered by setting the Ir–O CN to 3 in our model. This choice closely matches our experimental EXAFS results, which estimate the Ir–O coordination number to be ~3.01, as depicted earlier (*vide supra*). Such a coordination number is characteristic of tetrahedral sites in the spinel Co_3O_4 structure. Co atoms are typically coordinated to three or four oxygen atoms, depending on the lattice distortion and relaxation effects. Thus, we assigned Ir substitution at the tetrahedral Co site, as it best reproduces the local structure observed experimentally. The optimized crystal structure of the Ir-$_{SAC}$ Co_3O_4 system with Ir substitution at the tetrahedral Co site is illustrated in Fig. 6.

The defect formation energy (ΔE), as calculated using eqn (S1) (SI), substantiates the thermodynamic preference between tetrahedral and octahedral sites. The ΔE values for Ir-substituted tetrahedral and octahedral sites of Ir_{SAC}–Co_3O_4 are estimated to be −76.61 Ry and −73.44 Ry, respectively, suggesting a favorable structural configuration towards Ir substitution at the tetrahedral Co site with lower ΔE. This result also prioritizes consistency with the determined local atomic structure, which is critical for accurately representing the active site geometry of single-atom catalysts. Therefore, the tetrahedral substitution of Ir is both experimentally supported and structurally justified. In this context, it is noteworthy to mention that, within the present DFT framework, additional oxygen vacancies were initially introduced explicitly on the (001) plane of the bare Co_3O_4 system, as illustrated in Fig. S13. The calculated ΔE value for this O-vacant configuration is 79.92 Ry, and its positive magnitude indicates that the oxygen-deficient system is energetically less stable than the pristine Co_3O_4 lattice. Since the lattice parameters and atomic coordinates of the pristine Co_3O_4 structure were directly adopted from the experimentally refined crystallographic data, the model inherently reflects the intrinsic oxygen vacancy characteristics typically present in the spinel framework.[59] This modeling strategy ensures that the structural model realistically captures the defect environment observed in Co_3O_4-based systems, thereby maintaining close consistency with experimental conditions. Consequently, to avoid the artificial amplification of defect effects and to preserve the intrinsic electronic environment of the system, no additional oxygen vacancies were introduced in the calculations.

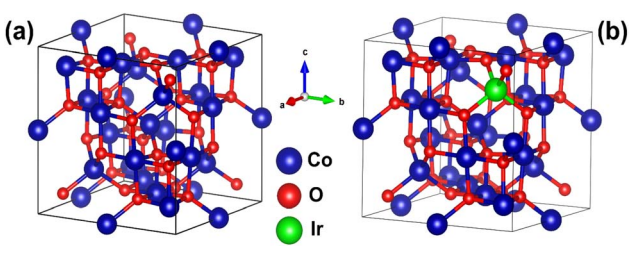

Fig. 6 Optimized crystal structures of (a) Co_3O_4 and (b) Ir_{SAC}–Co_3O_4 as obtained from DFT calculations.

5.2. Electronic characteristics of Co_3O_4 and Ir_{SAC}–Co_3O_4 systems

The electronic band structures (E–k diagrams) of Co_3O_4 and Ir_{SAC}–Co_3O_4 compounds, as estimated from the HSE functional, are shown in Fig. 7A and B, respectively, while the PBE functional is reported to underestimate the band gap (E_g) value of the Co_3O_4 system.[60–62] The PBE + Hubbard-U level of theory is known to overestimate the E_g value of the same compound[60,61] relative to the experimental result (E_g = 1.60 eV).[63] Considering the fact, the E_g values of the studied compounds have been calculated using the HSE functional with a screening parameter

value of 0.20. The HSE functional, in general, is recognized to predict the E_g values of the systems close to the experimental findings.[64–67] From Fig. 7A, it is observed that Co_3O_4 exhibits an indirect (direct) band gap opening along the X → W (X → X) high-symmetry direction with an E_g value of ~1.60 eV (1.64 eV). The E_g value of the compound, so attained from the HSE functional, is in good agreement with its experimental band gap, as reported by Shinde *et al.*[63] Interestingly, distinct band dispersions in the *E–k* diagram of the Ir_{SAC}–Co_3O_4 material are observed in Fig. 7B. The significant localization of electronic energy states on the Fermi energy level (E–E_F = 0 eV) indicates that Ir_{SAC}–Co_3O_4 is a conductor with an E_g value of 0 eV. The metallic behavior of Ir_{SAC}–Co_3O_4 further promotes the electron transfer efficiency and electrocatalytic activity towards the OER performance.[68–70]

The associated orbital-resolved PDOS of Co_3O_4 and Ir_{SAC}–Co_3O_4 compounds are depicted in Fig. 7a and b, respectively. The PDOS plots of the systems also reveal their respective semiconducting and metallic behaviors in line with the *E–k* diagrams [Fig. 7A and B]. In Fig. 7a, considerable asymmetries between the up- and down-spin channels of PDOS are reflected, which in turn result in a finite magnetic moment of 3.47 μ_B per cell. The magnetic moment of Co_3O_4, as attained from the HSE functional, is in close agreement with the experimental observation, as reported elsewhere.[58] Fig. 7a shows that while the up-spin channel of valence bands ranging from −1.5 to 0 eV for the Co_3O_4 system primarily originates from the Co^{3+}-4s, Co^{3+}-3d, Co^{2+}-4s and Co^{2+}-3d orbitals, while the down-spin channel mainly comes from the Co^{3+}-3d and Co^{2+}-3d orbitals. However, the weak contribution of the O-2p orbitals was also noticed on both the up- and down-spin channels of valence bands. The up- and down-spin channels of conduction bands ranging from 0–1.5 eV mostly consist of Co^{3+}-3d, Co^{2+}-3d, O-2p and Co^{3+}-3d, Co^{2+}-3d orbitals. Surprisingly, clear symmetries between the up- and down-spin channels of the PDOS spectra for the Ir_{SAC}–Co_3O_4 compound are portrayed in Fig. 7b. This observation shows an early indication of the antiferromagnetic behavior of the Ir_{SAC}–Co_3O_4 crystal system. In Fig. 7b, definite contribution of the Ir-5d atomic orbital is noticed in addition to the Co^{3+}-3d, Co^{2+}-3d and O-2p orbitals on both the up- and down-spin channels of PDOS. These results collectively suggest that Ir single-atom doping is vital in boosting the electrocatalytic performance of the Ir_{SAC}–Co_3O_4 compound, aligning well with our experimental results (*vide supra*). Additionally, upon the introduction of Ir single atoms, considerable Ir–O and Ir–Co interactions have been found to induce local structural relaxation, as evidenced from the orbital-resolved PDOS of the Ir_{SAC}–Co_3O_4 compound [Fig. 7b]. Owing to the larger atomic radius of Ir than that of O, local lattice distortion occurs, which can effectively suppress some pre-existing oxygen vacancies, thereby

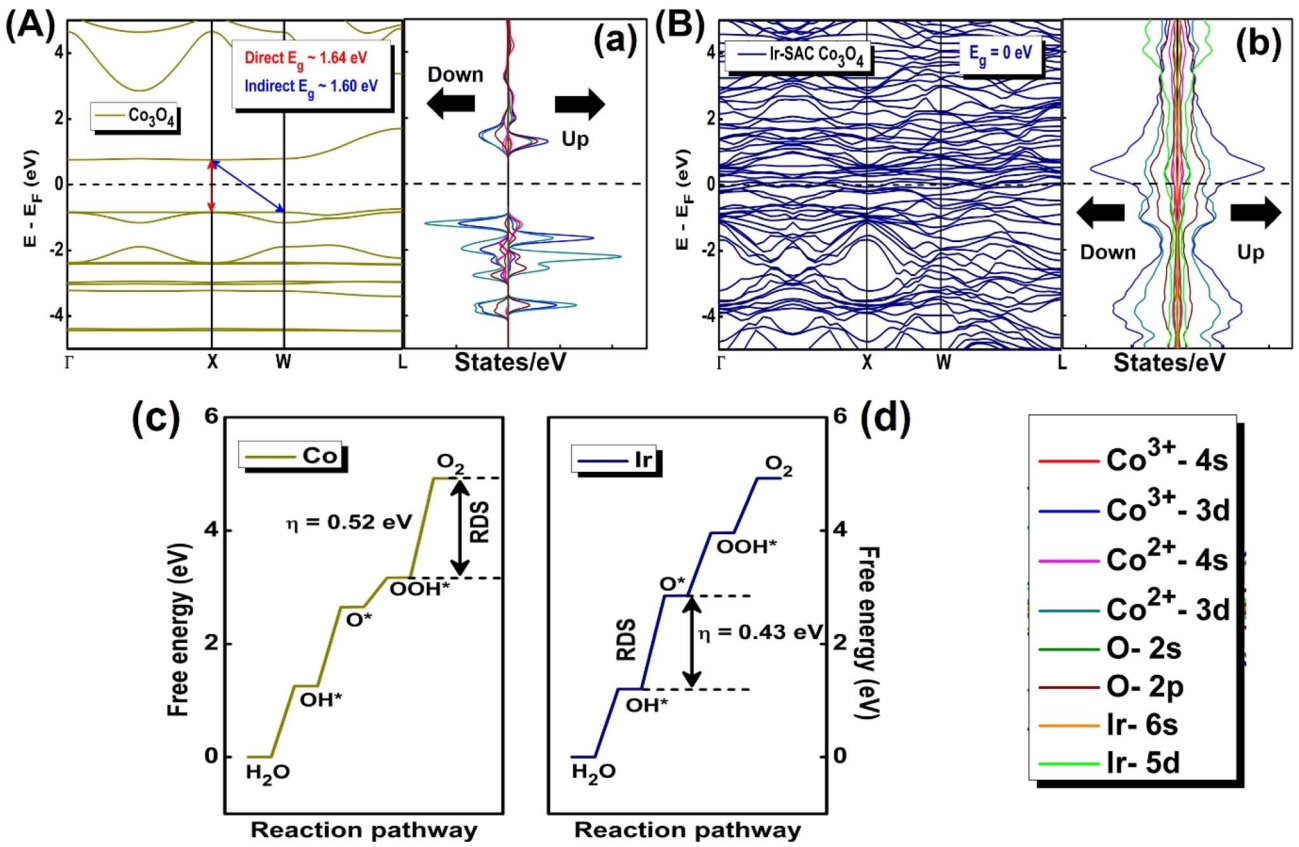

Fig. 7 Electronic band structures of (A) Co_3O_4 and (B) Ir_{SAC}–Co_3O_4 systems. Orbital-resolved PDOS plots of (a) Co_3O_4 and (b) Ir_{SAC}–Co_3O_4. [The Fermi energy level is marked at E–E_F = 0 eV. "Up" and "Down" represent the up spin and down spin states, respectively.]. Free energy *versus* OER pathways for (c) Co and (d) Ir atomic sites of the Co_3O_4 and Ir_{SAC}–Co_3O_4 systems, respectively.

lowering their concentration. Similar effects of single atom anchoring leading to vacancy passivation have been reported in other systems.[71,72] Importantly, despite the reduced oxygen-vacancy concentration, the electronic coupling between Ir atoms and the Co_3O_4 matrix introduces new electronic states and optimizes charge redistribution near the Fermi energy level [Fig. 7B(b)], which in turn may enhance the catalytic activity. Therefore, the increase in OER performance can be ascribed to the synergistic electronic effects and strong coordination of Ir atoms within the Co_3O_4 framework.

The modulation of the electronic structure upon Ir single-atom doping was further quantified through d-band center analysis derived from the PDOS. For pristine Co_3O_4, the d-band center values of Co^{3+} and Co^{2+} were located at −1.63 eV and −1.21 eV relative to the Fermi energy level, respectively, indicating relatively deep-lying d states consistent with its semiconducting nature, as also reflected in the *E*–*k* diagram and PDOS spectra (*cf.* Fig. 7). Upon the introduction of Ir single atoms, a pronounced shift of the d-band centers was observed, with Co^{3+} shifting to −1.05 eV and 0.44 eV, and Co^{2+} to −0.51 eV and 0.19 eV, while the Ir d-band center values were positioned close to the Fermi energy level (−0.22 eV and 0.29 eV). This significant shift toward the Fermi energy level is attributed to strong orbital hybridization among the Ir-5d, Co-3d, and O-2p states, as evidenced by the PDOS results, which show enhanced electronic states near the Fermi energy and a transition from semiconducting to metallic behavior. Such hybridization, coupled with charge redistribution from the metal centers to oxygen atoms, leads to the reorganization and broadening of the d states, thereby elevating their energy closer to the Fermi energy level. The upshifted d-band center may imply a strengthening of the interaction between the catalyst surface and oxygenated intermediates, facilitating improved adsorption of *OH and *OOH species while maintaining the favorable kinetics for *O formation and O–O bond coupling. Consequently, the optimized positioning of the d-band center in the Ir_{SAC}–Co_3O_4 matrix enables a balanced adsorption–desorption behavior, thereby enhancing the intrinsic electrocatalytic activity toward the oxygen evolution reaction. This analysis, in conjunction with the PDOS observations, confirms that the improved OER performance originates from the Ir-induced electronic structure modulation and synergistic coupling within the Co_3O_4 framework rather than solely from pristine Co_3O_4.

5.3. Charge transfer mechanism and Bader charge analyses in the Ir_{SAC}–Co_3O_4 system

To elucidate the electronic interaction between the Ir single atom and the Co_3O_4 matrix, Bader charge analysis was performed. Bader charge difference reveals that Ir and Co atoms undergo electron depletion of +0.86 e and +0.50 e, respectively, while oxygen atoms exhibit electron accumulation of −1.35 e. This charge redistribution indicates that electrons are transferred from the transition metal centers to the surrounding oxygen atoms, leading to the formation of electron-deficient Ir and Co species and electron-enriched O sites. Such behavior suggests that the incorporation of the Ir single atom induces significant electronic perturbation within the Co_3O_4 crystal system, with Ir acting as a dominant charge modulation center. The resulting charge polarization is facilitated through strong Ir–O–Co interactions, giving rise to enhanced metal–oxygen covalency and orbital hybridization. This interpretation is further supported by the orbital-resolved PDOS results (*vide supra*, *cf.* Section 5.2), wherein notable contributions from the Ir-5d states in conjunction with the Co-3d and O-2p orbitals near the Fermi energy level confirm strong electronic coupling and redistribution of electronic states upon Ir incorporation. The increased O-2p participation near the Fermi energy level is consistent with the observed electron accumulation on oxygen atoms, indicating improved charge delocalization across the lattice. Consequently, the formation of electron-rich oxygen sites is expected to promote proton-coupled electron transfer and stabilize the key OER intermediates (*OH and *OOH), while the electron-deficient Ir center may enhance the electrophilic character of the active site, facilitating *O formation and subsequent O–O bonding. In addition, the partial oxidation of Co sites further tunes the adsorption energetics, enabling an optimal balance between the intermediate binding strength and the reaction kinetics. Therefore, the enhanced OER activity of the Ir_{SAC}–Co_3O_4 compound is attributed to the synergistic electronic coupling and charge redistribution induced by the Ir single atom.

5.4. Electrochemical reaction pathway and active site(s) for the OER

To better understand the electrocatalytic water-splitting process and active site(s) for the OER, free energy changes were calculated as a function of the electrochemical reaction pathway. The calculations were performed for the Co and Ir atomic sites of Co_3O_4 and Ir_{SAC}–Co_3O_4 compounds, respectively. Fig. 7c and d show the results. Each site's overpotential (η) value was calculated for its rate-determining step (RDS). Although the RDS for the Co atomic site of Co_3O_4 can be estimated from the formation of O_2, the RDS for the Ir site of the Ir_{SAC}–Co_3O_4 system is correlated with the oxidation of OH* in the OER process.[73–75] From Fig. 7c and d, the η values of Co and Ir atomic sites in Co_3O_4 and Ir_{SAC}–Co_3O_4 systems were estimated to be 0.52 and 0.43 eV, respectively. The minimum η for the Ir site of the Ir_{SAC}–Co_3O_4 compound indicates the efficacy of Ir SAC as the predominant active site for the OER mechanism.

The binding energy difference of oxygen intermediates is directly linked with the η values of the atomic sites.[76] From Fig. 7c and d, the binding energy differences for OOH*–O_2 and OH*–O* intermediates of Co and Ir atomic sites along the reaction pathway were found to be 0.52 and 0.43 eV, respectively. This observation not only suggests that the Ir active site possesses a lower binding energy than the Co site but also shows that the estimated binding energy difference (=0.43 eV) falls under the optimal values of binding energy for the OER activity, as reported elsewhere.[77–80] The overall results portray that the Ir single atom doping on Co_3O_4 enhances the OER performance towards an improved electrocatalytic water-

splitting mechanism in line with the experimental observations (*vide supra*).

In this connection, it may be relevant to mention that the mechanistic interpretation of the OER pathway can also be correlated with experimental electrochemical data. The Tafel slope obtained for the Ir_{SAC}–Co_3O_4 system is 76 mV dec^{-1}, indicative of an RDS involving the OH*-to-O* conversion, as suggested by the classical electro kinetic models for the alkaline OER. This observation is in good agreement with the DFT results, which identify the OH* → O* transition as the RDS at the Ir site, with an associated overpotential of 0.43 eV, lower than that of the Co site in pristine Co_3O_4. The reduced energy barrier and optimized binding energy difference of OH*–O* at the Ir center suggest that Ir substitution enhances the OER kinetics by stabilizing the key intermediates and lowering the energy requirement for the rate-limiting step. This mechanistic correlation between theoretical predictions and experimental electrochemical data underscores the significance of Ir-SAC doping in promoting the OER activity.

6. Conclusions

To summarize, a three-step process was used to synthesize an Ir single-atom catalyst on a Co_3O_4 support. The first phase was the hydrothermal process, which involved the formation of a cobalt–carbonate–hydroxide complex, followed by the impregnation of Ir ions over the metal hydroxide complex and subsequently calcination, which resulted in Ir single atoms on the Co_3O_4 support. The XRD pattern of the synthesized sample confirmed the formation of the pure phase of Co_3O_4. Moreover, no diffraction peak corresponding to the IrO_2 and metallic Ir was observed. FESEM analysis confirmed a nanoflower morphology with edge lengths ranging from 100 to 400 nm. The vertically grown nanoflower morphology and rough surface were highly active for the electrocatalytic OER. Furthermore, the presence of single atoms was validated by HAADF-STEM images and XAS analysis. The HAADF-STEM mapping confirmed the atomic distribution of Ir single atoms on the substrate matrix. EXAFS analysis shows no peak of Ir–Ir bond for the Ir_{SAC}–Co_3O_4 sample, providing a strong affirmation for the presence of Ir single atoms. These single atoms stabilized on the Co_3O_4 support matrix *via* interaction with the support atoms and formed Ir–O and Ir–Co bond pairs. The bonding resulted in strong electronic coupling between the Ir single atoms and the Co_3O_4 matrix that modified the electronic state of Ir and led to its increased density of unoccupied orbitals. Furthermore, the valence state of Co atoms was enhanced by the electronic interaction with highly oxidized Ir single atoms, which further strengthened the overall electrocatalytic performance of the material. Consequently, the improved electrocatalytic OER efficiency emerged from the combined synergistic interaction of the support matrix and Ir single atoms. An adequate loading of Ir (3.02 wt%) was observed with the help of ICP-OES analysis. The synthesized Ir_{SAC}–Co_3O_4 showed improved OER activity in an alkaline medium, exhibiting an onset potential of 1.51 V *vs.* RHE to generate 10 mA cm^{-2} current density with a stability up to 96 h. This extended durability of Ir_{SAC}–Co_3O_4 demonstrated that Ir single atoms do not aggregate throughout the electrocatalysis. The calculated TOF value for Ir_{SAC}–Co_3O_4 was 0.03 s^{-1}, which was 15 times higher than that of the benchmark IrO_2. Post-electrocatalytic XPS analysis showed no substantial change in the oxidation state of Ir single atoms as well as Co atoms of the support matrix. Furthermore, post-electrocatalytic ICP-OES analysis confirmed no leaching of Ir atoms into the electrolyte. Both results demonstrated the robust electronic coupling between single atoms and the support matrix. The optimized binding energy values of intermediates during the OER calculated by DFT revealed an optimum binding energy for Ir sites, indicating that Ir is an active site for the OER. Therefore, this work demonstrated the anchoring of an Iridium single atom on a Co_3O_4 support with a strong synergistic electronic coupling, which indeed improves the electrocatalytic performance towards the OER under alkaline conditions.

Author contributions

Astha Gupta: conceptualization, overall research work, data acquisition, formal analysis, manuscript writing, and editing. Swarup Ghosh: computational work, writing and editing. Dinesh Bhalothia: data curation and formal analysis. Joydeep Chowdhury: writing and editing. Surojit Pande: overall design of research idea, data acquisition, formal analysis, supervision, funding acquisition, manuscript writing, and editing.

Conflicts of interest

The authors declare no conflicts of interest.

Data availability

All data supporting the findings of this study are available within the paper and its supplementary information (SI) file. Supplementary information: instrumental information, list of chemicals, calculation for all analyses, computational details, XRD patterns of samples, pristine Co_3O_4 and Ir single-atom-doped Co_3O_4, FESEM image, TEM image, and XPS spectrum of the pristine material, XAS fitting result, EPR analysis result, HAADF-STEM image, elemental mapping analysis, optimization of electrocatalytic activity, CV and C_{dl} measurements of Co_3O_4 and Ir_{SAC}–Co_3O_4, post-electrocatalysis FESEM, XPS, and Raman analyses, and crystal structure of the oxygen vacancy system.. See DOI: https://doi.org/10.1039/d6ta00849f.

Acknowledgements

Surojit Pande thanks the financial support from the Science and Engineering Research Board (SERB) under the sanction number CRG/2023/001368. Astha Gupta expresses gratitude to the BITS Pilani, Pilani campus, for their financial support. The authors would also like to thank the Central Instrument Facility (CIF) of BITS Pilani for granting access to the FESEM and XPS instruments. The researchers also acknowledge the Biology Department at BITS Pilani for carrying out the ICP analysis. They would also like to thank Dr Biplab Ghosh and Dr Rajashri

Urkude of the Raja Ramanna Centre for Advanced Technology (RRCAT) in Indore, India, for conducting the XAS analysis using the BL-09 Scanning EXAFS beamline, Indus-2 Synchrotron. They would like to acknowledge the SATHI Facility at IIT Kharagpur for the HAADF-STEM analysis. The authors would like to thank the National Supercomputing Mission (NSM) for providing the computing resources of 'PARAM Kamrupa' at IIT Guwahati, which is implemented by C-DAC and supported by the Ministry of Electronics and Information Technology (MeitY) and the Department of Science and Technology (DST), Government of India. Dinesh Bhalothia acknowledges the funding support (Enhanced Seed Grant EF/2024-25/QE-04-08) from Manipal University Jaipur. Swarup Ghosh would like to acknowledges Bioinformatics Resources and Applications Facility (BRAF), C-DAC, Pune for using a part of computational work.

References

1 D. Rathore, M. D. Sharma, A. Sharma, M. Basu and S. Pande, *Langmuir*, 2020, **36**, 14019–14030.
2 B. You and Y. Sun, *Acc. Chem. Res.*, 2018, **51**, 1571–1580.
3 N.-T. Suen, S.-F. Hung, Q. Quan, N. Zhang, Y.-J. Xu and H. M. Chen, *Chem. Soc. Rev.*, 2017, **46**, 337–365.
4 S. Anantharaj, S. R. Ede, K. Sakthikumar, K. Karthick, S. Mishra and S. Kundu, *ACS Catal.*, 2016, **6**, 8069–8097.
5 M. Kim, J. Park, M. Kang, J. Y. Kim and S. W. Lee, *ACS Cent. Sci.*, 2020, **6**, 880–891.
6 M. Basu, *J. Colloid Interface Sci.*, 2018, **530**, 264–273.
7 C. Mahala, M. D. Sharma and M. Basu, *Electrochim. Acta*, 2018, **273**, 462–473.
8 Y. Zhan, G. Du, S. Yang, C. Xu, M. Lu, Z. Liu and J. Y. Lee, *ACS Appl. Mater. Interfaces*, 2015, **7**, 12930–12936.
9 O. Diaz-Morales, I. Ledezma-Yanez, M. T. Koper and F. Calle-Vallejo, *ACS Catal.*, 2015, **5**, 5380–5387.
10 R. Elakkiya and G. Maduraiveeran, *Nanoscale*, 2021, **13**, 14837–14846.
11 Y. Guo, T. Park, J. W. Yi, J. Henzie, J. Kim, Z. Wang, B. Jiang, Y. Bando, Y. Sugahara and J. Tang, *Adv. Mater.*, 2019, **31**, 1807134.
12 G. Yuan, J. Bai, L. Zhang, X. Chen and L. Ren, *Appl. Catal., B*, 2021, **284**, 119693.
13 Z. Liu, X. Ning, A. Hao, M. F. Khan and S. Rehman, *ChemSusChem*, 2025, **18**, e202401197.
14 X. Xu, P. Du, Z. Chen and M. Huang, *J. Mater. Chem. A*, 2016, **4**, 10933–10939.
15 F. Abdelghafar, X. Xu, D. Guan, Z. Lin, Z. Hu, M. Ni, H. Huang, T. Bhatelia, S. P. Jiang and Z. Shao, *ACS Mater. Lett.*, 2024, **6**, 2985–2994.
16 X. Xu, Y. Pan, L. Ge, Y. Chen, X. Mao, D. Guan, M. Li, Y. Zhong, Z. Hu, V. K. Peterson, M. Saunders, C.-T. Chen, H. Zhang, R. Ran, A. Du, H. Wang, S. P. Jiang, W. Zhou and Z. Shao, *Small*, 2021, **17**, 2101573.
17 X.-F. Yang, A. Wang, B. Qiao, J. Li, J. Liu and T. Zhang, *Acc. Chem. Res.*, 2013, **46**, 1740–1748.
18 L. Liu and A. Corma, *Chem. Rev.*, 2018, **118**, 4981–5079.
19 H. Zhang, G. Liu, L. Shi and J. Ye, *Adv. Energy Mater.*, 2018, **8**, 1701343.
20 J. Li, G. Fu, X. Sheng, G. Li, H. Chen, K. Shu, Y. Dong, T. Wang and Y. Deng, *Adv. Powder Mater.*, 2024, **3**, 100227.
21 T. Wei, J. Zhou and X. An, *Mater. Rep. Energy*, 2024, **4**, 100285.
22 Y. Zhou, Y. Jiang, Y. Ji, R. Lang, Y. Fang and C. D. Wu, *ChemCatChem*, 2023, **15**, e202201176.
23 J. Li, C. Chen, L. Xu, Y. Zhang, W. Wei, E. Zhao, Y. Wu and C. Chen, *JACS Au*, 2023, **3**, 736–755.
24 M. B. Gawande, P. Fornasiero and R. Zbořil, *ACS Catal.*, 2020, **10**, 2231–2259.
25 Q. Wang, Z. Zhang, C. Cai, M. Wang, Z. L. Zhao, M. Li, X. Huang, S. Han, H. Zhou and Z. Feng, *J. Am. Chem. Soc.*, 2021, **143**, 13605–13615.
26 P. Zhai, M. Xia, Y. Wu, G. Zhang, J. Gao, B. Zhang, S. Cao, Y. Zhang, Z. Li and Z. Fan, *Nat. Commun.*, 2021, **12**, 4587.
27 A. Gupta, S. Ghosh, D. Bhalothia, S. Thangarasu, B. Ghosh, R. Urkude, J. Chowdhury and S. Pande, *J. Mater. Chem. A*, 2024, **12**, 23819–23836.
28 R. Lang, X. Du, Y. Huang, X. Jiang, Q. Zhang, Y. Guo, K. Liu, B. Qiao, A. Wang and T. Zhang, *Chem. Rev.*, 2020, **120**, 11986–12043.
29 R. Li, L. Luo, X. Ma, W. Wu, M. Wang and J. Zeng, *J. Mater. Chem. A*, 2022, **10**, 5717–5742.
30 K. Tan, M. Dixit, J. Dean and G. Mpourmpakis, *Ind. Eng. Chem. Res.*, 2019, **58**, 20236–20246.
31 Z. Yan, B. Yao, C. Hall, Q. Gao, W. Zang, H. Zhou, Q. He and H. Zhu, *Nano Lett.*, 2022, **22**, 8122–8129.
32 B. He, P. Hosseini, T. Priamushko, O. Trost, E. Budiyanto, C. Bondue, J. Schulwitz, A. Kostka, H. Tüysüz, M. Muhler, S. Cherevko, K. Tschulik and T. Li, *Nat. Commun.*, 2025, **16**, 9895.
33 R. Zhang, L. Pan, B. Guo, Z.-F. Huang, Z. Chen, L. Wang, X. Zhang, Z. Guo, W. Xu, K. P. Loh and J.-J. Zou, *J. Am. Chem. Soc.*, 2023, **145**, 2271–2281.
34 A. Kumar, M. Gil-Sepulcre, J. P. Fandré, O. Rüdiger, M. G. Kim, S. DeBeer and H. Tüysüz, *J. Am. Chem. Soc.*, 2024, **146**, 32953–32964.
35 M.-Q. Yang, K.-L. Zhou, C. Wang, M.-C. Zhang, C.-H. Wang, X. Ke, G. Chen, H. Wang and R.-Z. Wang, *J. Mater. Chem. A*, 2022, **10**, 25692–25700.
36 C. Cai, M. Wang, S. Han, Q. Wang, Q. Zhang, Y. Zhu, X. Yang, D. Wu, X. Zu and G. E. Sterbinsky, *ACS Catal.*, 2020, **11**, 123–130.
37 J. Shan, C. Ye, S. Chen, T. Sun, Y. Jiao, L. Liu, C. Zhu, L. Song, Y. Han and M. Jaroniec, *J. Am. Chem. Soc.*, 2021, **143**, 5201–5211.
38 W. Zhao, F. Xu, J. Yang, X. Hu and B. Weng, *Inorg. Chem.*, 2024, **63**, 1947–1953.
39 D. Bhalothia, Y.-M. Yu, Y.-R. Lin, T.-H. Huang, C. Yan, J.-F. Lee, K.-W. Wang and T.-Y. Chen, *Sustainable Energy Fuels*, 2021, **5**, 5490–5504.
40 P. Hu, Z. Huang, Z. Amghouz, M. Makkee, F. Xu, F. Kapteijn, A. Dikhtiarenko, Y. Chen, X. Gu and X. Tang, *Angew. Chem., Int. Ed.*, 2014, **53**, 3418–3421.
41 N. Cheng, S. Stambula, D. Wang, M. N. Banis, J. Liu, A. Riese, B. Xiao, R. Li, T.-K. Sham and L.-M. Liu, *Nat. Commun.*, 2016, **7**, 13638.

42 L. Zhang, R. Si, H. Liu, N. Chen, Q. Wang, K. Adair, Z. Wang, J. Chen, Z. Song and J. Li, *Nat. Commun.*, 2019, **10**, 4936.
43 J. Yin, J. Jin, M. Lu, B. Huang, H. Zhang, Y. Peng, P. Xi and C.-H. Yan, *J. Am. Chem. Soc.*, 2020, **142**, 18378–18386.
44 L. Liu, Z. Jiang, L. Fang, H. Xu, H. Zhang, X. Gu and Y. Wang, *ACS Appl. Mater. Interfaces*, 2017, **9**, 27736–27744.
45 S. Biswal, B. Mishra, D. Pohl, B. Rellinghaus, D. Ghosh and B. P. Tripathi, *J. Mater. Chem. A*, 2024, **12**, 2491–2500.
46 D. Rathore, S. Ghosh, A. Gupta, J. Chowdhury and S. Pande, *ACS Appl. Nano Mater.*, 2024, **7**, 9730–9744.
47 K. L. Zhou, Z. Wang, C. B. Han, X. Ke, C. Wang, Y. Jin, Q. Zhang, J. Liu, H. Wang and H. Yan, *Nat. Commun.*, 2021, **12**, 3783.
48 B. He, F. Bai, P. Jain and T. Li, *Small*, 2025, **21**, 2411479.
49 C. Lin, Y. Zhao, H. Zhang, S. Xie, Y.-F. Li, X. Li, Z. Jiang and Z.-P. Liu, *Chem. Sci.*, 2018, **9**, 6803–6812.
50 P. Li, M. Wang, X. Duan, L. Zheng, X. Cheng, Y. Zhang, Y. Kuang, Y. Li, Q. Ma and Z. Feng, *Nat. Commun.*, 2019, **10**, 1711.
51 Q. He, S. Qiao, Q. Zhou, Y. Zhou, H. Shou, P. Zhang, W. Xu, D. Liu, S. Chen and X. Wu, *Nano Lett.*, 2022, **22**, 3832–3839.
52 S. Yagi, I. Yamada, H. Tsukasaki, A. Seno, M. Murakami, H. Fujii, H. Chen, N. Umezawa, H. Abe, N. Nishiyama and S. Mori, *Nat. Commun.*, 2015, **6**, 8249.
53 R. Madhu, A. Karmakar, P. Arunachalam, J. Muthukumar, P. Gudlur and S. Kundu, *J. Mater. Chem. A*, 2023, **11**, 21767–21779.
54 C. Pasquini, L. D'Amario, I. Zaharieva and H. Dau, *J. Chem. Phys.*, 2020, 152.
55 B. S. Yeo and A. T. Bell, *J. Am. Chem. Soc.*, 2011, **133**, 5587–5593.
56 J. Huang, H. Sheng, R. D. Ross, J. Han, X. Wang, B. Song and S. Jin, *Nat. Commun.*, 2021, **12**, 3036.
57 W. L. Smith and A. D. Hobson, *Acta Crystallogr., Sect. B*, 1973, **29**, 362–363.
58 W. L. Roth, *J. Phys. Chem. Solids*, 1964, **25**, 1–10.
59 Z.-H. Yin, H. Liu, J.-S. Hu and J.-J. Wang, *Natl. Sci. Rev.*, 2024, **11**, nwae362.
60 J. Chen, X. Wu and A. Selloni, *Phys. Rev. B:Condens. Matter Mater. Phys.*, 2011, **83**, 245204.
61 I. Kim, H.-H. Nahm and M. Choi, *Curr. Appl. Phys.*, 2021, **22**, 65–70.
62 A. F. Lima, *J. Phys. Chem. Solids*, 2014, **75**, 148–152.
63 V. R. Shinde, S. B. Mahadik, T. P. Gujar and C. D. Lokhande, *Appl. Surf. Sci.*, 2006, **252**, 7487–7492.
64 S. Ghosh and J. Chowdhury, *RSC Adv.*, 2024, **14**, 6385–6397.
65 S. Ghosh and J. Chowdhury, *Mod. Phys. Lett. B*, 2023, **38**, 2330003.
66 S. Ghosh and J. Chowdhury, *Mater. Sci. Eng., B*, 2022, **284**, 115903.
67 S. Ghosh, S. Sarkar and J. Chowdhury, *Mater. Chem. Phys.*, 2022, **276**, 125379.
68 D. Rathore, S. Ghosh, A. Gupta, J. Chowdhury and S. Pande, *ACS Appl. Nano Mater.*, 2024, **7**, 9730–9744.
69 D. Rathore, S. Ghosh, J. Chowdhury and S. Pande, *ACS Appl. Nano Mater.*, 2023, **6**, 3095–3110.
70 D. Rathore, S. Ghosh, J. Chowdhury and S. Pande, *ACS Appl. Nano Mater.*, 2022, **5**, 11823–11838.
71 X. Wang, D. Santos-Carballal and N. H. de Leeuw, *J. Chem. Phys.*, 2024, **160**, 154713.
72 S. Chandrappa, S. J. Galbao, P. S. Sankara Rama Krishnan, N. A. Koshi, S. Das, S. N. Myakala, S.-C. Lee, A. Dutta, A. Cherevan, S. Bhattacharjee and D. H. K. Murthy, *J. Phys. Chem. C*, 2023, **127**, 12383–12393.
73 N. Dubouis and A. Grimaud, *Chem. Sci.*, 2019, **10**, 9165–9181.
74 M. Irshad, M. H. U. R. Mahmood and M. Fatima, in *Graphene, Nanotubes and Quantum Dots-Based Nanotechnology*, ed. Y. Al-Douri, Woodhead Publishing, 2022, pp. 537–556.
75 S. F. Zai, X. Y. Gao, C. C. Yang and Q. Jiang, *Adv. Energy Mater.*, 2021, **11**, 2101266.
76 B. You, M. T. Tang, C. Tsai, F. Abild-Pedersen, X. Zheng and H. Li, *Adv. Mater.*, 2019, **31**, 1807001.
77 B. Hinnemann, P. G. Moses, J. Bonde, K. P. Jørgensen, J. H. Nielsen, S. Horch, I. Chorkendorff and J. K. Nørskov, *J. Am. Chem. Soc.*, 2005, **127**, 5308–5309.
78 I. C. Man, H.-Y. Su, F. Calle-Vallejo, H. A. Hansen, J. I. Martínez, N. G. Inoglu, J. Kitchin, T. F. Jaramillo, J. K. Nørskov and J. Rossmeisl, *ChemCatChem*, 2011, **3**, 1159–1165.
79 S. Sun, X. Zhou, B. Cong, W. Hong and G. Chen, *ACS Catal.*, 2020, **10**, 9086–9097.
80 J. Li, *Nano-Micro Lett.*, 2022, **14**, 112.

